



RESEARCH ARTICLE

10.1029/2021JF006332

Special Section:

Modeling in glaciology

Modeling the Deformation Regime of Thwaites Glacier, West Antarctica, Using a Simple Flow Relation for Ice Anisotropy (ESTAR)

F. S. McCormack^{1,2} , R. C. Warner³ , H. Seroussi^{4,5} , C. F. Dow⁶ , J. L. Roberts⁷ , and A. Treverrow⁷ 

Key Points:

- Flow relations that account for tertiary creep and anisotropy change the simulated contributions of deformation and sliding to overall flow
- Ice in tertiary creep is softer leading to increased simulated vertical shear deformation where bed parallel shear stresses dominate
- How flow relations account for anisotropy influences the simulated contributions of longitudinal and transverse stresses in momentum balance

Supporting Information:

Supporting Information may be found in the online version of this article.

Correspondence to:

F. S. McCormack,
felicity.mccormack@monash.edu

Citation:

McCormack, F. S., Warner, R. C., Seroussi, H., Dow, C. F., Roberts, J. L., & Treverrow, A. (2022). Modeling the deformation regime of Thwaites Glacier, West Antarctica, using a simple flow relation for ice anisotropy (ESTAR). *Journal of Geophysical Research: Earth Surface*, 127, e2021JF006332. <https://doi.org/10.1029/2021JF006332>

Received 26 JUN 2021

Accepted 16 FEB 2022

¹School of Earth, Atmosphere & Environment, Monash University, Clayton, VIC, Australia, ²Institute for Marine and Antarctic Studies, University of Tasmania, Hobart, TAS, Australia, ³Australian Antarctic Program Partnership, Institute for Marine and Antarctic Studies, University of Tasmania, Hobart, TAS, Australia, ⁴Thayer School of Engineering, Dartmouth College, Hanover, NH, USA, ⁵Jet Propulsion Laboratory, California Institute of Technology, Pasadena, CA, USA, ⁶Department of Geography and Environmental Management, University of Waterloo, Waterloo, ON, Canada, ⁷Australian Antarctic Division, Kingston, TAS, Australia

Abstract Ice deformation dominates the evolution of ice shelf flow and the slow-moving regions in the interior of ice sheets. However, deformation may be poorly represented in large-scale ice sheet models that use the Glen flow relation, due to its questionable applicability to the steady-state flow of anisotropic ice that prevails in ice sheets, having been derived from secondary creep rates of isotropic ice. We assess the deformation regimes of Thwaites Glacier, West Antarctica, using the Glen and “Empirical Scalar Tertiary Anisotropy Regime”, (ESTAR) flow relations, the latter being derived from steady-state deformation rates of anisotropic ice. For grounded ice, the character of the flow relation determines the contribution of deformation to overall flow, with ESTAR producing greater bed-parallel shear deformation than the standard Glen flow relation. The ESTAR experiments show larger basal shear stress maxima than the standard Glen experiment because ESTAR treats the responses to simple shear stresses and compression stresses differently, reducing the role of lateral and longitudinal stresses in momentum balance. On the Thwaites Glacier Tongue, ESTAR provides the best match to observed speeds by accounting for the differing effects of stresses on ice flow. Our results highlight the importance of the numerical description of anisotropy, particularly: In regions of transition from deformation-dominated to sliding-dominated flow; in the approach to the grounding line, and across ice shelves. Given the importance of these locations in determining mass flux into the ocean, our results have implications for projections of sea level change from Antarctic ice loss.

Plain Language Summary Glacial ice flows by stress-driven deformation, involving movement within and between ice crystals, and also by sliding at the bedrock in the presence of meltwater. The rate of deformation in large-scale models of polar ice sheets is usually described by the Glen flow relation, which is limited in how appropriately it describes deformation in the long-term, nearly steady flows typical of ice sheets. We compare modeling of the deformation regimes of Thwaites Glacier, West Antarctica, using the Glen and Empirical Scalar Tertiary Anisotropy Regime (ESTAR) flow relations. ESTAR was formulated to represent more realistically the deformation rates that occur under prolonged stress, where the orientations of individual ice crystals develop into significantly organized patterns. ESTAR predicts more vertical shear deformation than the Glen relation, leading to faster flow over most of the Thwaites catchment, and particularly in slow-moving regions in the interior where modeling with the Glen relation predicts unrealistic sliding. ESTAR also provides a better match to the observed surface speeds on the floating Thwaites Glacier Tongue. Our results highlight how improved descriptions of deformation change the distribution of stresses and the relative contributions of deformation and sliding to overall ice flow.

1. Introduction

Ice sheets flow by a combination of ice deformation and basal sliding. Basal sliding dominates flow in fast-moving regions, where basal meltwater is present, and in regions with easily deformed beds, and is assumed to be the dominant process contributing to ice mass flux across the grounding line (e.g., Rignot, 2001; Rignot et al., 2011). Bed-parallel vertical simple shear deformation near the bed dominates flow in regions where basal temperatures are below the ice pressure melting point and the bed resists deformation. Deformation by lateral and longitudinal

© 2022. The Authors.

This is an open access article under the terms of the [Creative Commons Attribution-NonCommercial-NoDerivs License](https://creativecommons.org/licenses/by/4.0/), which permits use and distribution in any medium, provided the original work is properly cited, the use is non-commercial and no modifications or adaptations are made.

stresses also plays a critical role in ice shelves, including in buttressing the flow of upstream ice and in the deglaciation of marine ice sheets (Hindmarsh, 2006; Weertman, 1974). Incorporating physically realistic descriptions of both deformation and sliding in numerical models is therefore key to accurately simulating the evolution of ice sheets and predicting their contribution to sea level rise over the coming century and beyond.

Our understanding of the role of deformation in ice flow has progressed in recent decades, facilitated by: advances in inverse modeling capabilities for inferring ice deformation parameters (C. P. Borstad et al., 2013); the increasing availability of datasets constraining physical characteristics of ice and their spatial variability (e.g., Faria et al., 2014a; Jordan et al., 2019; Smith et al., 2017; Treverrow et al., 2016); and both numerical modeling and laboratory-based experiments in ice mechanics for constraining flow relations (e.g., Budd et al., 2013; Faria et al., 2014b; Minchew et al., 2018; Placidi & Hutter, 2006; Treverrow et al., 2012). However, the contribution of deformation to overall ice flow is not well constrained due to: (a) Uncertainties in the theory (Marshall, 2005), (b) challenges in implementing complex microstructural processes into numerical models (Graham et al., 2018), (c) a paucity of observations that constrain the relative contributions of basal sliding and deformation to the overall ice flow (e.g., Maier et al., 2019), and (d) the challenges associated with selecting appropriate flow parameter values for modeling glaciers and ice sheets (e.g., Zeitz et al., 2020). Disentangling the relative contributions of deformation and basal sliding to ice motion is made more complicated by the fact that ice deformation plays an essential role in the way that stresses are distributed englacially and at the basal boundary, for example, the role of lateral and longitudinal stresses in modulating the basal shear stress extrema.

The flow relation most commonly used in large-scale ice sheet models has its origins in the prolific work of Glen (Glen, 1952, 1953, 1955, 1958; Nye, 1953). What is nowadays commonly termed “the Glen flow relation” was developed from laboratory experiments on isotropic polycrystalline ice and applies to the transient conditions of secondary (minimum) creep (Budd et al., 2013). It is conventionally (e.g., Cuffey & Paterson, 2010; Paterson, 1994) taken to have a cubic nonlinearity, following (Glen, 1955). However, tertiary (steady-state) creep is the predominant mode of deformation in ice sheets and glaciers (e.g., the discussion in Graham et al., 2018). Under prolonged deformation to tertiary creep, anisotropic crystal orientation fabrics develop that are compatible with the character of the applied stresses, and the action of these stresses on the anisotropic ice leads to enhanced ice flow rates (Budd et al., 2013; Budd & Jacka, 1989; Li et al., 1996; Warner et al., 1999). Crucially these rates depend on the character of the applied stresses. The Glen flow relation is inherently unable to take account of these enhanced flow rates.

Given that under prolonged deformation polycrystalline ice develops an anisotropic character, it is clear that to predict deformation rates a flow relation needs to connect the anisotropy with the orientation of the applied stresses. This requires expressions involving more than just the deviatoric stress tensor. Other flow relations directly introduce vectors that characterize the material anisotropy (e.g., Gillet-Chaulet et al., 2005; Placidi et al., 2010) or directly use individual crystal *c*-axes (e.g., Azuma & Goto-Azuma, 1996). Such models can of course predict the deformational responses of any given aggregate of crystal orientations to an arbitrary applied stress field. An alternative to the Glen flow relation, the ESTAR flow relation (Empirical Scalar Tertiary Anisotropy Regime), was recently proposed (Budd et al., 2013; Graham et al., 2018). ESTAR uses the assumption of microstructural compatibility with the stress configuration. Ice flowing in ice sheets generally progresses through slowly changing patterns of applied stresses, so ESTAR focuses on modeling the deformation rates applicable under the assumption that the current pattern of stresses has prevailed long enough to produce compatible anisotropy. Accordingly, ESTAR only requires information about the prevailing pattern of stresses and knowledge of the relevant tertiary flow rates for that situation, and takes as an additional ingredient, beyond the stress and strain-rate tensors is the shear fraction λ_s , which characterizes the proportion of the deformation that constitutes ongoing simple shear. Through the assumption of microstructural compatibility with the stress configuration, ESTAR avoids the requirement to explicitly evolve the ice crystal orientation fabric to determine the influence of anisotropy on the flow, and is as computationally tractable as the Glen flow relation (Graham et al., 2018).

The aim of this study is to examine differences in the modeled deformation regimes of a real-world glacier system arising from using the ESTAR and Glen flow relations. We consider the Thwaites Glacier catchment, which is one of the most well-observed regions in Antarctica (Scambos et al., 2017). Thwaites Glacier has been rapidly evolving over recent decades, including losing mass, thinning, accelerating, and showing substantial grounding line retreat (Gardner et al., 2018; Milillo et al., 2019; Mougnot et al., 2014; Paolo et al., 2015; Rignot, 2008), and has the potential to make a significant contribution to future sea level rise (Joughin et al., 2014; Scambos

et al., 2017; Seroussi et al., 2017). Hence, it is critically important for estimates of Thwaites' contribution to sea level rise to determine the balance of dynamics contributing to the overall flow of this system, and how these dynamics depend on the flow relation. We particularly aim to understand how and why the relative contributions of deformation and sliding flow differ depending on the flow relation. In Section 2 we present an overview of the ESTAR and Glen flow relations; Section 3 details the model setup, datasets, and experiments; Sections 4 and 5 present and discuss the results; and Section 6 provides a summary and outlook.

2. ESTAR Flow Relation

The origins, derivation, underlying assumptions, and some limitations of the ESTAR flow relation are discussed in detail in Budd et al. (2013) and Graham et al. (2018). First, we give an overview of the conceptual framework behind ESTAR (Section 2.1), then present the ESTAR equations (Section 2.2), which describe how the relative proportions of simple shear and deviatoric normal stresses modulate the deformation rates, and discuss the differences between the ESTAR and Glen flow relations.

2.1. ESTAR Conceptual Overview

The ESTAR flow relation constitutes a development in approaches to describing the effect of compatible crystallographic anisotropy on the deformation rates of ice in steady-state or tertiary flow by reference to the character of the applied stresses (see e.g., Budd et al., 2013 and the review by; Marshall, 2005). The previous applications involved specific deformation geometries or focused on particular aspects of deformation (such as enhanced flow rates for bed-parallel shear in ice sheet modeling). By contrast, Budd et al. (2013) present results from a series of laboratory ice deformation experiments involving combined compression and simple shear stresses performed at -2°C , mostly at effective stresses of ~ 0.5 MPa, and carried out to the tertiary flow regime. They confirmed the results of Li et al. (1996) that the enhancement of deformation rates (relative to the minimum creep rate of isotropic ice) systematically increased as the relative importance of simple shear increased. Budd et al. (2013) remarked this was also reflected in the individual shear and compression strain rates, and accordingly proposed a generalization to arbitrary stress configurations—what Graham et al. (2018) termed ESTAR. The enhanced tertiary flow rates are largely achieved at more modest strains than those required to develop a full steady-state fabric. Through a functional interpolation between the enhancement factors for compression alone and simple shear alone, ESTAR captures the responses to a range of applied stress patterns acting on the corresponding compatible anisotropic distributions of crystal orientations. Budd et al. (2013) give an overview of the theoretical underpinning of the ESTAR flow relation as well as presenting representative crystal orientation fabrics, together with detailed discussions connecting the crystal orientation fabrics and the observed deformation rates.

Clearly for the ESTAR flow relation to be applicable at temperatures relevant to ice sheets the connections between the patterns of applied stresses, the developed compatible crystallographic anisotropies, and their responses to stresses need to remain applicable. The topic of experimental tertiary flow rate enhancement factors for compression, and possible dependence on both temperature and stress, has a long history (see e.g., Jacka & Jun 2000). Stress dependence also appears connected with different power law exponents for secondary creep in isotropic ice and tertiary flow (Treverrow et al., 2012), which complicates some interpretation of high stress studies. For simple shear, laboratory experiments indicate that the steady-state or compatible crystal fabric is a single maximum for temperatures above about -20°C , with crystal *c*-axes strongly clustered about the normal to the plane on which the shear stress acts (see e.g., Budd & Jacka, 1989; Qi et al., 2019). There is some evidence that the strength of this clustering decreases by -30°C (Qi et al., 2019).

For uniaxial compression there are competing processes in the evolution of crystal orientations: lattice rotation involved with the deformation tends to move *c*-axes toward the axis of the compressive stress, while temperature dependent processes such as migration recrystallization tend to create crystals at 45° to that axis. At temperatures above about -20°C this competition generates “small-circle girdle” fabrics at steady-state, with a peak density of crystal *c*-axis orientations in a ring at less than 45° to the compression axis, and considerably fewer crystals at larger angles. This has been observed in laboratory studies (Budd & Jacka, 1989; Craw et al., 2018; Dahl-Jensen et al., 1997; Fan et al., 2020) and in some Antarctic ice cores (see e.g., Budd & Jacka, 1989). The forms of compatible fabrics for simple shear and uniaxial compression both prove to be more deformable than isotropic

ice under the corresponding stresses, but exhibit different levels of enhancement, presumably due to differences in the proportions of favorably oriented crystals.

As temperatures decrease, the “girdle angle” of compressive fabrics decreases (Fan et al., 2020), and experiments at -30°C (performed at high stresses: $\sim 4\text{--}8\text{ MPa}$ Craw et al., 2018; Fan et al., 2020) show this peak feature disappearing and the distribution being replaced by a broad solid cone of c -axes, at moderate strains ($\sim 20\%$), while still indicating enhanced flow rates. Recent modeling of fabric evolution (Richards et al., 2021) reproduces these behaviors and suggests that at -25°C the girdle opening angle does not close until more than 50% axial strain. Evidence from deep ice cores from East Antarctica (Lipenkov et al., 1989; Weikusat et al., 2017) where ice has been deformed to even greater axial strains under temperatures ranging from -50°C to -30°C under much lower stresses and in apparently low shear environments, shows the rotational effect dominating, resulting in ice that is reported by Pimienta et al. (1987) as much stiffer than isotropic ice under the prevailing deformation patterns.

We will return to the question of relevant compatible crystal orientation fabrics when discussing our choice of shear and compression enhancement factors for ESTAR in Section 2.2.

2.2. ESTAR Equations

The ESTAR flow relation is given by the following expression

$$\dot{\epsilon} = A(T') E(\lambda_S) \tau_e^{n-1} \sigma', \quad (1)$$

and the Glen flow relation can be written

$$\dot{\epsilon} = A(T') E_G \tau_e^{n-1} \sigma'. \quad (2)$$

In both of these equations, $\dot{\epsilon}$ is the strain rate tensor (s^{-1}); σ' is the deviatoric stress tensor (Pa); and τ_e is the effective stress (Pa)—The square root of the second invariant of the deviatoric stress tensor, given by $\tau_e = \sqrt{\text{tr}(\sigma'^2)/2}$. The term n is the power law stress exponent, here using the common $n = 3$. The factor $A(T')$ is a temperature-dependent flow parameter ($\text{Pa}^{-3} \text{s}^{-1}$) based on the minimum creep rate of isotropic ice, where T' is the temperature relative to the pressure dependent melting point of ice (Greve et al., 2014). In ice sheet modeling it is more convenient to work with the dynamic viscosity, which connects deviatoric stresses to strain rates ($\sigma' = 2\eta\dot{\epsilon}$) and which for Equation 1 is given by $\eta = 1/2[A(T') E(\lambda_S) \tau_e^{n-1}]^{-1}$. We use coordinates x , y , and z , where z is vertical (i.e., gravity acts downwards). In discussing the character of the deviatoric stress tensor it is sometimes convenient to express the components with respect to a local orthonormal reference frame (\hat{v} , \hat{t} , \hat{z}) where \hat{v} is the direction of flow, \hat{t} is transverse to flow (\hat{v} and \hat{t} are denoted the “horizontal” coordinates), and \hat{z} is vertical. In what follows, we refer to the longitudinal and transverse normal stresses—The σ'_{vv} and σ'_{tt} components of the deviatoric stress tensor σ' —And the “horizontal” simple shear stress σ'_{vt} as “membrane stresses” (in accordance with common practice, see e.g., Hindmarsh, 2006).

The key difference between the ESTAR and Glen flow relations is in the specification of the dimensionless enhancement factors $E(\lambda_S)$ and E_G . For ESTAR, the term $E(\lambda_S)$ accounts for the different enhancement factors for tertiary deformation rates, compared to the secondary deformation rate for isotropic ice, depending on the combination of simple shear and deviatoric normal stresses. Accordingly it has a coherent spatial variation. The term $E(\lambda_S)$ is parametrized by the shear fraction λ_S (Budd et al., 2013):

$$E(\lambda_S) = E_C + (E_S - E_C) \lambda_S^2. \quad (3)$$

Here, the terms E_C and E_S are the constant enhancement factors for compression and simple shear alone, respectively. The difference in enhancement factors is obviously central to the ESTAR relation. The overall deformation rate also involves uncertainties in $A(T')$ the temperature-dependent rate factor at minimum creep. It should also be remembered that crystallographic anisotropy is not necessarily the only reason for tertiary flow rates to differ from minimum creep rates. The shear fraction λ_S in Equation 3 describes the proportion of simple shear to effective stress. This term ranges from 0 (for compression alone) to 1 (for simple shear alone), and is given by the following expression:

$$\lambda_S = \frac{\tilde{\tau}}{\tau_e}. \quad (4)$$

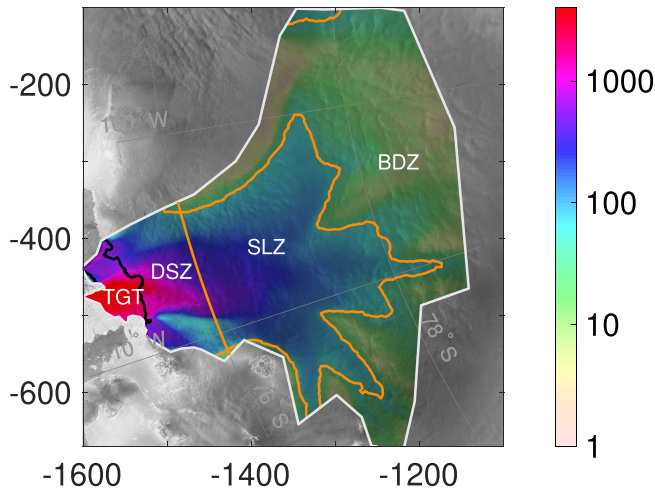


Figure 1. Thwaites Glacier model domain with observed velocities in color (m yr^{-1} on log scale; Rignot et al., 2011; Rignot et al., 2017), overlaid on RADARSAT 200 m resolution imagery (Jezek & Team, 2002). The black line is the grounding line, and the Thwaites Glacier Tongue is the western portion of the ice shelf. The 50 m yr^{-1} surface speed contour—that delineates the shear margins and the transitions from high to low bed topography (Raymond et al., 2001) and from strong/hard to weak/deformable beds (Joughin et al., 2009)—is shown in orange, as is the 76°S line of latitude. The mixed deformation-sliding zone, the sliding zone, and the bed-parallel vertical simple shear deformation zone (BDZ) are marked (delineated by the orange lines). The model uses WGS 84/Antarctic polar stereographic coordinates referenced to the 71°S latitude; the x - and y -axis labels are in units of km.

Here, $\bar{\tau}$ is the magnitude of the shear stress (Pa) on the local non-rotating shear plane, the entity that defines simple shear in the “movement picture” approach to treating deformation flow (Budd et al., 2013; Duval, 1981; Kamb, 1972; Li et al., 1996; Warner et al., 1999). It has long been known that in prolonged deformation it is possible to discriminate ongoing simple shear from normal (compressive or tensile) deformations, by considering the velocity field as well as the tensors describing the deformation. Kamb (1972) referred to this as requiring consideration of the “movement picture” as used in structural petrology, while Duval (1981) referred to the presence of a “permanent shear plane.” Recognizing (following Kamb, 1972) that in contrast to laboratory experiments this shear plane changes its orientation along flow in real applications, Budd et al. (2013) refer to the “local non-rotating shear plane.” This plane represents a local set of adjacent planes slipping past each other where ice is locally undergoing simple shear as it flows (combined with any simultaneous normal deformations along or across flow). Projections of the deviatoric stresses or strain-rates onto this plane permit the identification of the shear fraction λ_s . Clearly this plane should contain the velocity vector, and Budd et al. (2013) pointed out that it should also contain that part of the vorticity vector of the flow (the curl of the velocity field, $\nabla \times v$) associated solely with deformation, that is, excluding any local rigid body rotations (also suggested by Kamb, 1972). Graham et al. (2018) presented a pragmatic approach to isolating this deformational vorticity, including the assumption that there was no contribution from swirling flow around stream lines.

The ESTAR flow relation Equation 1 is collinear, which means that, as for the Glen flow relation, the deviatoric stresses in the ESTAR flow relation are related to the corresponding strain rates by a simple scalar relationship—That is, collectively, the term $A(T') E(\lambda_s) \tau_e^2$ is scalar. Hence, λ_s can be written equivalently in terms of strain rates:

$$\lambda_s = \frac{\dot{\epsilon}'}{\dot{\epsilon}_e}, \quad (5)$$

where $\dot{\epsilon}'$ is the magnitude of the strain rate (s^{-1}) on the local non-rotating shear plane, and $\dot{\epsilon}_e$ is the effective strain rate (s^{-1}). We refer to the square of the shear fraction (λ_s^2), that interpolates between E_c and E_s in Equation 3, as the shear parameter.

In Equation 2, E_G is a constant enhancement factor that does not distinguish between proportions of simple shear and normal deviatoric stresses. E_G was not part of the original Glen flow relation; we include E_G in Equation 2 to facilitate comparison with the ESTAR flow relation. Many ice sheet modeling studies have similarly included an enhancement factor in the Glen flow relation (e.g., Aschwanden et al., 2013; Bindschadler et al., 2013; Greve & Hutter, 1995; Huybrechts & Oerlemans, 1988; Martin et al., 2011). These enhancement factors are often essentially tuning parameters that may lack the physical basis to differentiate between conditions of secondary and tertiary creep, the effects of temperature and impurities, damage, and other microstructural properties that influence ice deformation, and to account for the anisotropic, and hence spatially and temporally (e.g., as a result of grounding line migration) variable, nature of ice flow (see e.g., Greve & Blatter, 2009).

3. Ice Sheet Modeling

3.1. Model Setup and Datasets

We use ISSM—a three-dimensional thermomechanical ice sheet model (Larour et al., 2012) – building on a model of the Thwaites Glacier catchment by Seroussi et al. (2017) with the domain shown in Figure 1. The mesh comprises a total of 228,915 prismatic elements over 10 vertical layers, with edge lengths as small as 500 m in the fast-flowing areas. The mesh is generated using static adaptive mesh refinement (Larour et al., 2012) based on observed surface speeds (Rignot et al., 2011, 2017). For our diagnostic, thermomechanical simulations (see

Section 3.2), we use the three-dimensional model from Blatter (1995) and Pattyn (2003)—the Blatter-Pattyn (BP) model—for momentum balance, and the thermal model from Aschwanden et al. (2012), as implemented in ISSM (Seroussi et al., 2013).

The bed topography, ice thickness, and grounding line data are derived from Morlighem et al. (2020). The surface temperature field is from RACMO2.3 (Lenaerts et al., 2012) (see Section 3.2 below) and the geothermal heat flux from Ståhl et al. (2021). Friction is applied at the ice-bed interface according to the Budd-type relation (Budd et al., 1979). The friction coefficient in this relation is determined using inverse methods (Morlighem et al., 2010) and observed surface velocities (Rignot et al., 2011, 2017). We limit rapid spatial variations in the friction coefficient by including a Tikhonov regularization term in the cost function for the inversion. The strength of the regularization is determined using an L-curve analysis (Hansen, 2000). Further details of this method and the L-curve analysis are provided in Text S2 in Supporting Information S1.

We use the (Budd & Jacka, 1989) parameterization for the temperature-dependent flow rate $A(T)$ in Equation 1. The sensitivity of our results to this formulation compared with those of (Cuffey & Paterson, 2010) and (Paterson, 1994) is shown in the Text S3 in Supporting Information S1. We have chosen not to calculate a spatially-varying $A(T)$ using inverse methods on the ice shelf so that we can directly compare the impact of the different enhancement factors on the modeled ice flow. The absence of any tuning of the dynamics increases the mismatch between the observed and modeled velocities on the ice shelf, and is larger than the agreement achieved for the grounded ice sheet where basal friction acts as a control parameter, as discussed below and in Text S3 in Supporting Information S1.

3.2. Numerical Experiments

The aim of this study is to evaluate the differences in the modeled flow regimes of Thwaites Glacier that arise as a consequence of the different treatment of deformation in the ESTAR and Glen flow relations. We run diagnostic experiments for Thwaites Glacier with the relevant enhancement factors: $E(\lambda_s)$ for the ESTAR flow relation, and E_G for the Glen flow relation.

For the ESTAR flow relation we chose the ratio $E_C/E_S = 3/8$, consistent with the value used in a comparative study of several anisotropic flow relations (Treverrow et al., 2015). Values for E_S ranging from ~ 3 to 12 can be found in the literature (see e.g., Budd et al., 2013; Treverrow et al., 2012). Budd and Jacka (1989) estimated $E_S = 8$, while Pimienta et al. (1987) suggest $E_S \sim 10$, a value that is used in parameterizing the anisotropic flow model of Gillet-Chaulet et al. (2005), (2006), and the CAFFE model (Placidi et al., 2010), another scalar generalization of the Glen relation. In this study we take $E_S = 5$ as an appropriate shear enhancement for tertiary flow at stress magnitudes relevant to polar ice masses (0.1 MPa), based on an assessment of laboratory experiments that explored the apparent stress dependence of enhancement factors (Treverrow et al., 2012). This leads to a compressive enhancement factor $E_C = 15/8$ which, while lower than the estimates of $E_C = 3$ from laboratory studies (e.g., Budd & Jacka, 1989), is more consistent with values from Treverrow et al. (2012) for 0.1 MPa, and might also be more appropriate at ice sheet temperatures. However, the values of these enhancement factors, and how they might vary with stress magnitude and temperature, deserves further investigation. We refer to the experiments using the ESTAR flow relation as the E5 experiments.

It is less straightforward to compare the ESTAR choice of E_C with the inputs to most other models. This is because ESTAR only predicts deformation rates for compatible fabrics, while models that can predict deformation rates for stresses applied to arbitrary crystal orientation fabrics involve different considerations. For example, they aim to capture the extreme stiffness associated with uniaxial compression on strong single maxima, while they would still predict relatively enhanced flow for a small-circle girdle fabric. Indeed the CAFFE model of Placidi et al. (2010) sets its maximum stiffness at an effective enhancement factor of 0.1 simply to avoid numerical complications. Pimienta et al. (1987) report $E_C = 0.4$ for uniaxial compression on an ice sample with a strong single maximum fabric, from an experiment at -15°C at a deformation of 1% strain, where very little evolution of fabric would be expected. As discussed above, we regard that as an incompatible pairing of stress and anisotropy at that temperature.

For the Glen flow relation, we consider the case when $E_G = 5$ (termed the G5 experiment), since choosing $E_G = E_S$ should minimize the differences between E5 and G5 in regions where the flow is controlled by bed-parallel vertical simple shear deformation (Graham et al., 2018). We also perform experiments choosing $E_G = 1.94$ (the

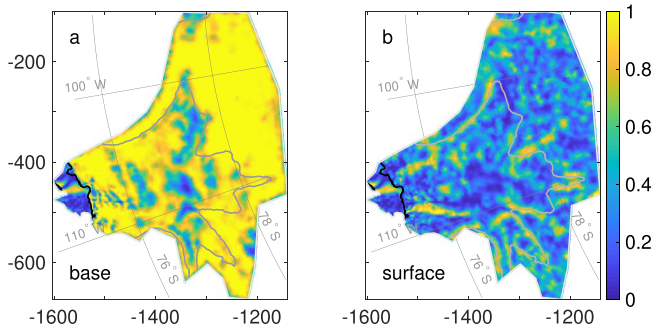


Figure 2. E5 shear parameter λ_s^2 at the ice sheet a base and b surface. The black line is the grounding line and the gray line is the 50 m yr⁻¹ surface speed contour.

value that minimizes the median percentage difference between observed and simulated surface speeds over the Thwaites Glacier Tongue; termed the G2 experiment) and $E_G = 1$ (the G1 or standard Glen flow relation experiment).

As a first step, we calculate basal friction coefficients using inversion and the shallow shelf approximation for each flow relation. Using these basal friction coefficients, for each flow relation we calculate steady-state 3D velocity distributions using the BP model (see Text S1 in Supporting Information S1) and temperature distributions using the Aschwanden et al. (2012) enthalpy formulation of the thermal model, as detailed in Seroussi et al. (2013). A comparison of the basal thermal regimes for the flow relations is provided in Text S4 in Supporting Information S1, along with an overview of the thermal model equations. We then use inverse methods to calculate basal friction coefficients, and we compare the resulting flow and stress distributions derived from these experiments for each flow relation. Given our inverse modeling approach, the surface velocities over grounded ice will be similar

for each flow relation. This enables us to directly compare the internal stress configurations and relative contributions of basal sliding and deformation to ice motion as a result of differences in the flow relations.

We do not test the sensitivity of our results to the value of the flow exponent n (Bons et al., 2016). Laboratory studies indicate that n varies from ~ 3 in the secondary creep stage to ~ 4 in tertiary creep (Glen, 1952, 1953, 1955; Qi et al., 2017; Treverrow et al., 2012). In our experiments, $n = 3$ to be consistent with the laboratory experiments and analytical framework underpinning the ESTAR flow relation (Budd et al., 2013; Treverrow et al., 2012, 2015). Further investigation into appropriate values for these parameters in both laboratory and modeling studies is warranted.

4. Results

4.1. The ESTAR Shear Fraction λ_s

To frame the context for the differences in the deformation regimes modeled using each flow relation, we first consider how the shear parameter λ_s^2 varies spatially and from the ice sheet base to the surface in the E5 experiment.

On grounded ice, the near-bed stress configuration is generally dominated by simple shear ($\lambda_s^2 \approx 1$; Figure 2a). This indicates that bed-parallel shear is the dominant regime for a large portion of Thwaites catchment. For ESTAR, $E(\lambda_s) \approx 5$ in these regions, with a corresponding strongly enhanced deformation rate near the bed (Section 4.3). Significant coherent exceptions to basal $\lambda_s^2 \approx 1$ can be seen downstream of the 50 m yr⁻¹ speed contour, indicating the dominance of normal stresses associated with the loss of basal traction (Section 4.3). Localized deviations from simple shear-dominated basal stress configurations also occur in the fast-flowing region in proximity to the grounding line. These are strongly connected to the derived basal shear stresses.

The significant stresses present in the near-surface ice are vertical normal deviatoric stresses (typically compressive) and the membrane stresses (σ'_{vv} , σ'_{tt} , σ'_{vt}). Hence, near the surface, the normal to the local non-rotating shear plane lies in the horizontal plane orthogonal to the flow direction, and the shear fraction λ_s^2 reflects the relative importance of the shear stress component aligned with the flow (σ'_{vt}) compared with the effective stress.

The surface values of λ_s^2 (Figure 2b) are generally low (< 0.5), indicating that the predominant surface stresses are the along- and across-flow normal deformations (Figure S7a and S7b in Supporting Information S1). Exceptions to this are along the shear margins of the flow where coherent stripes of shear dominance can be clearly seen. The stress configuration in the shear margins is shear-dominated throughout the column, typically transitioning from shear membrane stresses at the surface (Figure S7c in Supporting Information S1) to bed-parallel vertical shear near the bed. Other small regions of high surface λ_s^2 not aligned with shear membrane stresses exist (e.g., where multiple streams merge), reflecting the complexity of the three-dimensional flow.

The essentially plug nature of ice shelf flow (i.e., no vertical shear) means that the surface λ_s^2 field is representative of the stress configuration profiles through the entire shelf thickness (Figures 2a and 2b). Over most of the Thwaites Glacier Tongue (TGT), flow- and aligned normal stresses dominate ($\lambda_s^2 \ll 0.5$), and the TGT

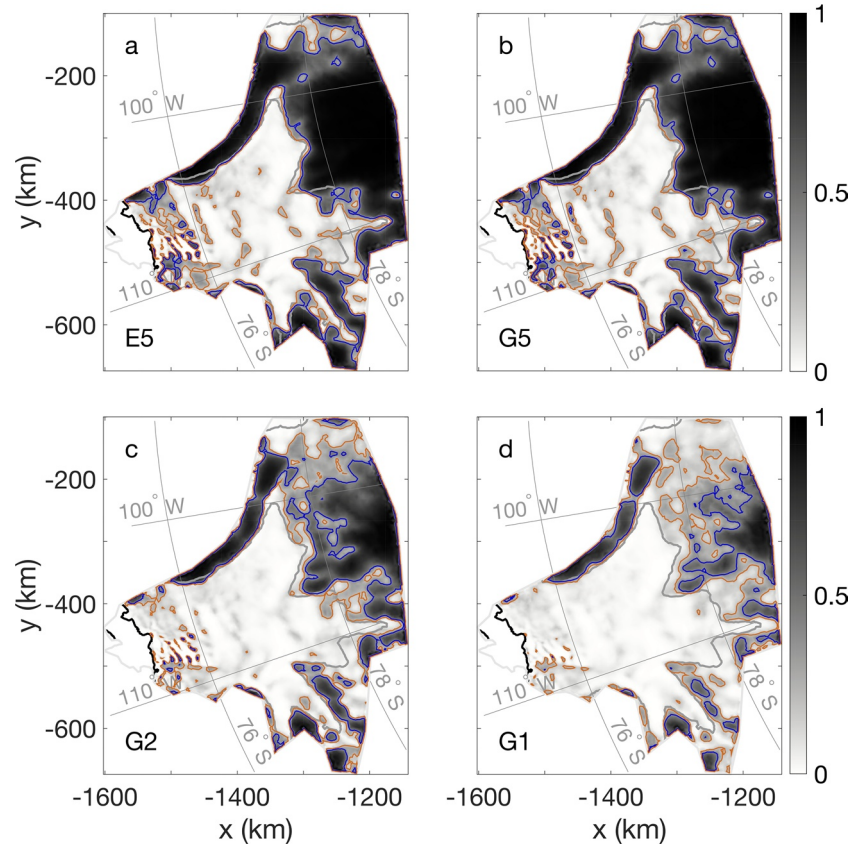


Figure 3. Deformation speed fractions, that is, the relative contribution of deformation (v_d) to total surface speed (v), for: (a) E5; (b) G5; (c) G2; and (d) G1. The black and gray lines are the same as in Figure 2. The orange and blue lines are the 0.2 and 0.4 deformation speed fraction contours, respectively.

area-averaged E5 enhancement factor is $E(\lambda_S) = 2.54$. Simple shear flow dominates the stress configuration ($\lambda_S^2 > 0.5$) in other parts of the ice shelf, including the eastern margin of the TGT, as well as the zone upstream of the major pinning point on the eastern portion of the shelf.

4.2. Deformation and Sliding on Grounded Ice

We next examine the relative contributions of deformation and sliding to the overall flow over grounded ice for each flow relation. Our diagnostic results provide insights into how these two processes combine to control the observed flow because we have constrained the basal friction coefficients to minimize the mismatch between modeled and observed surface velocities for each flow relation.

We partition the total surface velocity v into basal sliding v_s and deformational v_d components:

$$v = v_s + v_d. \quad (6)$$

This local characterization of deformational flow by v_d essentially captures the role of bed-parallel shear. It indirectly reflects the influence of the spatial variations of membrane stresses, which influence the vertical shear through momentum balance and contribute to the pattern of basal shear stress.

The relative contribution of bed-parallel shear to total surface speed ($|v_d|/|v|$, henceforth the deformation speed fraction) is shown in Figure 3. Naturally, v_d (Figures 4a, 4d and 4g and 4j) is strongly correlated ($r = 0.85$ for E5, $r = 0.83$ for G5, $r = 0.84$ for G2, and $r = 0.86$ for G1) with the cube of the corresponding basal shear stress (Figures 4b, 4e and 4h and 4k). However, the magnitude of v_d and the corresponding patterns in the deformation

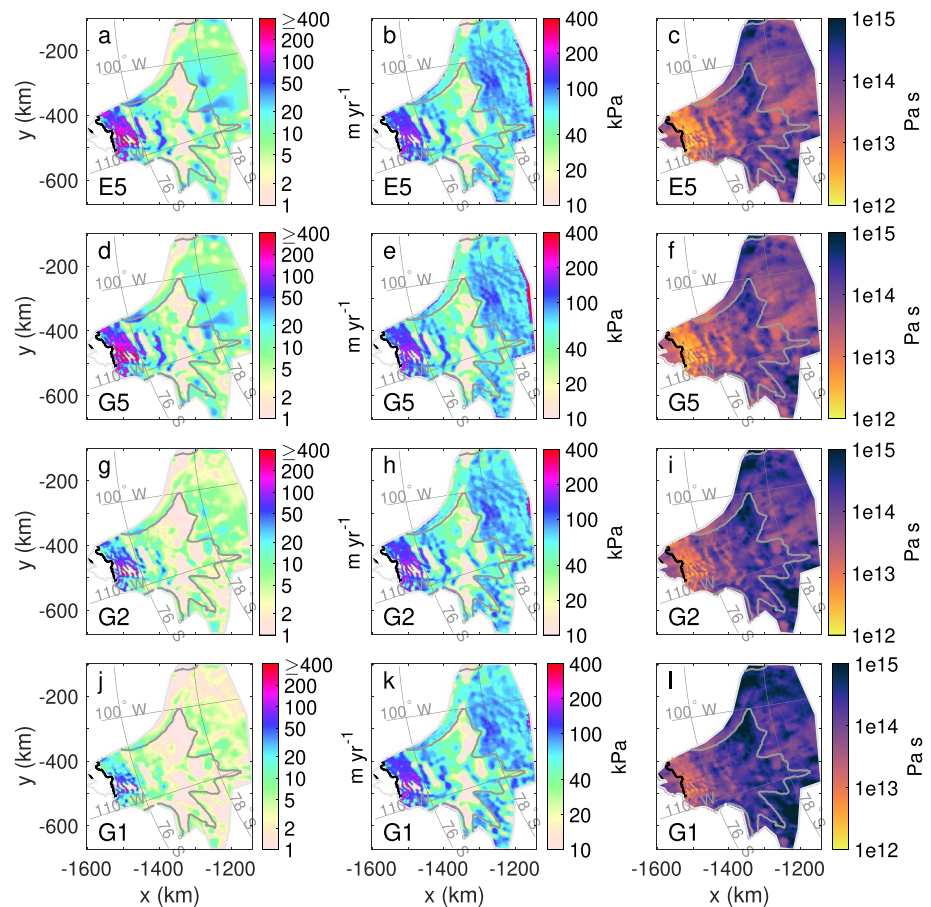


Figure 4. Component of surface speeds associated with deformation (v_d ; m yr^{-1}) for (a) E5; (d) G5; (g) G2; and (j) G1. Basal shear stresses (kPa) for (b) E5; (e) G5; (h) G2; and (k) G1. Surface viscosities (Pa s) for (c) E5; (f) G5; (i) G2; and (l) G1. The black and gray lines in each panel are the same as in Figure 2. Note the log color axes in each panel.

speed fraction (Figure 3) are directly linked to the magnitude of the prescribed enhancement parameter relevant to each flow relation. We find a median of 57.6% more deformational contribution to surface velocity in E5 than G1; 38.2% more from deformation in E5 than G2; and 8.7% less from deformation in E5 than G5.

Examining the E5 deformation speed fraction over grounded ice (Figure 3a), three distinct flow regimes emerge. First, in the catchment interior where surface speeds are $<50 \text{ m yr}^{-1}$, the deformation speed fraction is generally high (the area-averaged value for E5 is 0.76; Table 1), indicating that bed-parallel shear dominates flow there. We denote this region as the bed-parallel shear deformation zone (BDZ; Figure 1).

Second, an abrupt transition in the deformation speed fraction for the E5 experiment occurs at the $\sim 50 \text{ m yr}^{-1}$ surface speed contour, marking a transition from deformation-dominated to sliding-dominated flow. Here, and extending to the $\sim 76^\circ\text{S}$ line of latitude, the E5 deformation speed fraction is generally very low (the area-averaged value is 0.05). We denote this region the sliding zone (SLZ). It is clear that even where simple shear deformation dominates the stress configuration in the basal layers (Figure 2a), this does not imply the dominance of v_d in the overall flow (Figure 3a). Basal sliding in the SLZ is occasionally accompanied by a loss of shear dominance in the basal layer, linked to almost vanishing basal traction (Figure 4b), as discussed below.

Finally, in the $\sim 80 \text{ km}$ immediately upstream of the grounding line (i.e., north of $\sim 76^\circ\text{S}$), the E5 deformation speed fraction increases, and is greater

Table 1
Median Deformation Surface Speed (v_d ; m yr^{-1}) and Deformation Speed Fraction (v_d/v) for Each Flow Relation, by Dynamic Regime

	E5		G5		G2		G1	
	v_d	v_d/v	v_d	v_d/v	v_d	v_d/v	v_d	v_d/v
BDZ	9.33	0.76	9.55	0.77	4.99	0.40	3.11	0.24
SLZ	5.76	0.05	6.56	0.06	3.28	0.03	2.16	0.02
DSZ	46.49	0.20	49.29	0.20	24.13	0.10	15.70	0.06

than 0.4 in highly localized zones oriented perpendicular to the flow direction. We denote this mixed regime of deformation and sliding the deformation-sliding zone (DSZ). Localized stripes of alternating high and low v_d in the DSZ (and of a much smaller magnitude in the SLZ) arise from alternating patterns of extrema in basal shear stresses that have been previously reported (e.g., Joughin et al., 2009; Sergienko & Hindmarsh, 2013; Sergienko et al., 2014).

Differences between the E5 and the G5, G2, and G1 deformation speed fractions directly depend on differences in the level of enhancement of bed-parallel shear in the near basal part of the ice column. As expected, the G5 deformation speed fraction closely matches that of E5 across the domain, although the G5 experiment predicts slightly more deformation over grounded ice than the E5 experiment (Table 1). This is consistent with: (a) Basal $\lambda_s^2 \approx 1$, so that $E(\lambda_s) \approx E_G$ in most regions of bed-parallel shear; (b) stiffer E5 ice in the upper layers of the ice sheet where surface $\lambda_s^2 < 1$, and accordingly $E(\lambda_s) < E_G$; and (c) less extreme E5 basal shear stress magnitudes than G5 (Figures 4b and 4e), as discussed below.

The deformation speed fractions for G2 and G1 (Figure 3c and 3d) are everywhere smaller than the E5 (and G5) case, as expected given the reduced magnitude of the enhancement parameters in these experiments. The largest differences between the E5 deformation speed fractions and those of G2 and G1 occur in the BDZ and DSZ. The magnitude of the reduction in deformation speed fractions is most marked for G1, where deformation contributes less than 10% to overall flow for more than half of the grounded ice sheet. In the BDZ, where the E5 and G5 experiments predict median deformation speed fractions of >0.75 , the G2 deformation speed fraction is 0.4, and the G1 deformation speed fraction is 0.24, indicating sliding-dominated flow with these two experiments.

4.3. Stress Configuration on Grounded Ice

We next examine the stresses giving rise to the different controls on flow identified above for each flow relation.

As expected under the common driver of surface slope, the magnitudes of the basal shear stresses generally agree between the flow relations (Figures 4b, 4e, 4h and 4k). For each flow relation, zones of almost vanishing basal shear stresses are apparent in the SLZ and also in highly localized regions in the DSZ. The latter are regions where the local driving stress opposes the flow. In all these zones of very low basal shear stress, the driving stress is not balanced locally at the bed by the basal shear stress. Instead, the membrane stress terms clearly complete the momentum balance here, with variations in normal stresses (particularly longitudinal ones) dominating (Figure 2b). There are strong correlations between low membrane stress magnitudes (e.g., Figure S6c in Supporting Information S1 for E5) with their corresponding relatively stiff ice (high surface viscosities) and the zones of low basal shear stress for all flow relations (compare Figures 4c, 4f, 4i and 4l with Figures 4b, 4e, 4h and 4k).

The extrema of the basal shear stresses are modulated to a lesser extent by the enhancement factors in the flow relation via the membrane stresses. The importance of the membrane stresses (relative to the basal shear stresses) in momentum balance increases with increasing ice stiffness (as reflected by the surface viscosity), which itself increases for decreasing enhancement factor (see the ratios in Figures 5a, 5c and 5e).

Considering the differences in the stress configurations of the E5 and G5 experiments, we find that the E5 ice is stiffer than the G5 ice outside the regions where simple shear dominates (i.e., everywhere $\lambda_s^2 < 0.5$ in Figure 2). This applies to much of the upper part of the ice sheet (Figure 5a) where the E5 membrane stresses play a greater role in momentum balance compared with the G5 membrane stresses. Indeed, the extremes of the E5 basal shear stresses are reduced compared to G5: the G5 – E5 difference is generally positive over basal shear stress maxima and negative over basal shear stress minima (compare the differences in basal shear stresses, Figure 5b, with the stresses themselves, Figures 4b and 4e). The magnitudes of the differences between the G5 and E5 basal shear stresses increase downstream to the DSZ where the largest differences occur.

The sign of the difference between E5 and G2 basal shear stresses is reversed compared with G5, with the G2 ice being almost everywhere stiffer than the E5 ice and the G2 membrane stresses generally playing a greater role in momentum balance than those of E5 throughout the catchment. This is as expected due to the surface values of λ_s for E5, and as shown by the ratio of surface viscosities (Figure 5c). Similar findings hold for the differences between E5 and G1, although the magnitude of the difference is even greater since the G1 ice is even stiffer than the G2 ice.

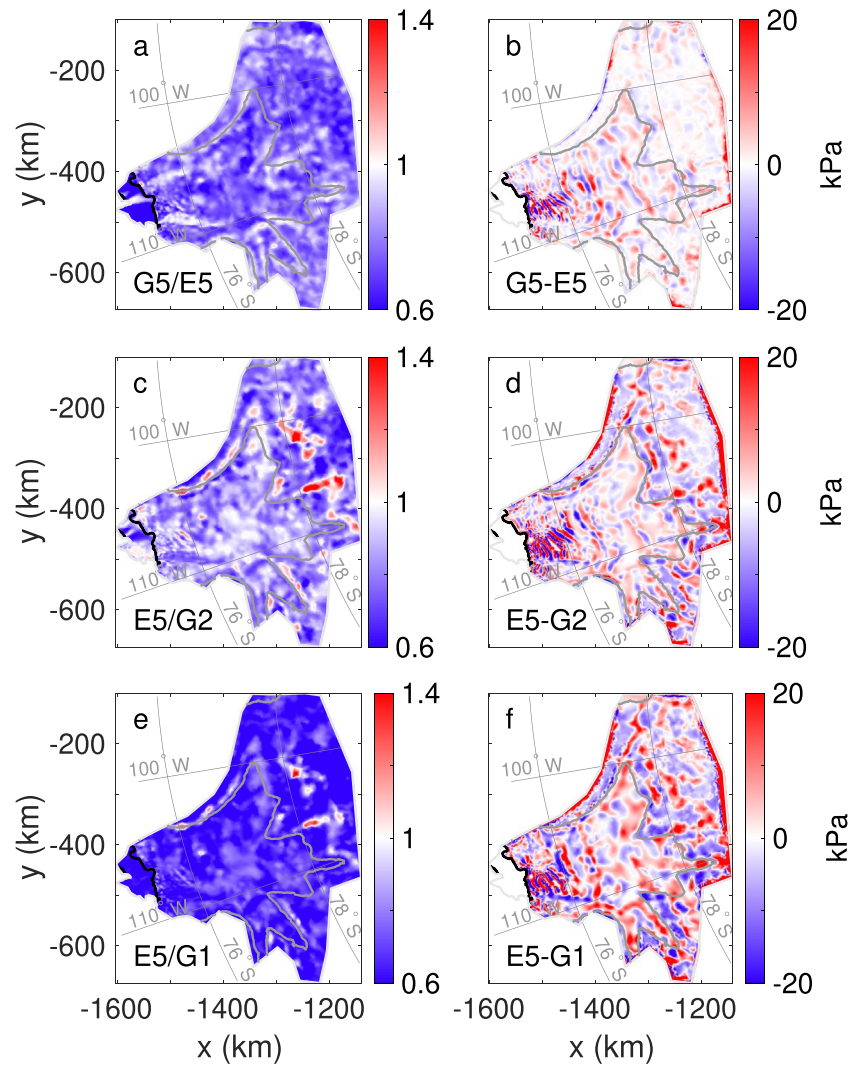


Figure 5. Ratio of surface viscosities for a G5/E5; (c) E5/G2; and (e) E5/G1. Difference between the basal shear stresses (kPa) for (b) G5 – E5; (d) E5 – G2; and (f) E5 – G1. The first-mentioned flow relation in each pairing generally has softer ice and more extreme variations in basal shear stresses. The black and gray lines in each panel are the same as in Figure 2.

4.4. Ice Shelf Flow

Lastly, we consider the impact of the underlying stress configurations on the modeled ice shelf flow. As we have chosen to use a prescribed flow rate parameter rather than calculate $A(T')$ using inverse methods, we can directly compare the impact of the different enhancement factors on the modeled ice flow (Text S3 in Supporting Information S1). In particular, since the ice shelf flow is not locally controlled by the inversion for basal friction, the comparison with observations provides direct insight into the complete flow relations, including $A(T')$. As a result, we see larger mismatches between the observed and modeled velocities on the ice shelf than over grounded ice, as expected.

Delineating the fast-flowing TGT (see Figure 1) from the eastern shelf by the 1,000 m yr^{-1} surface speed contour, the observed TGT surface speeds are, on average, 5.03 times greater than those of the eastern shelf (the ratio of median surface speeds is 13.98). Over most of the TGT, the E5 experiment provides the best match to observed surface speeds (Table 2, Figure 6). By contrast, the G5 experiment tends to overestimate while G2 and G1 tend to underestimate the TGT surface speeds. The degree of mismatch between observed and modeled surface speeds increases for the Glen flow relations as the difference between the relevant enhancement factor and the ESTAR TGT area-averaged value of $E(\lambda_G) = 2.54$ increases (Section 4.1).

Table 2
Area-Averaged Mean and Median Percentage Difference Between Modeled and Observed Surface Speeds for the Thwaites Glacier Tongue and Ee

	E5		G5		G2		G1	
	median	rmse	median	rmse	median	rmse	median	rmse
TGT	1.84	431	29.21	1,296	-2.25	487	-17.78	675
Eastern shelf	57.35	446	102.97	759	54.30	428	33.83	367
Total	10.36	437	44.57	1,111	9.35	466	-6.05	576

These results are related to the impact of each of the flow relations on the ice stiffnesses, and any dependence on the underlying stress configuration. For E5, by accounting for the separate effects of extensional and simple shear stresses through $E(\lambda_s)$, the E5 ice stiffnesses vary across the TGT as a function of the stress configuration (Figure 2), leading to a better match to ice surface speeds. Flow-aligned normal stresses dominate across much of the TGT so that the G5 experiment, with the enhancement factor of $E_G = 5$, results in ice that is everywhere softer (Figure 5a) and faster-flowing (Figure 6a and 6b) than E5. The ice in the G2 experiment is stiffer than the E5 case wherever $E(\lambda_s) < 1.94$, but softer where normal stresses dominate (Figure 5c), which leads to an underestimation of surface speeds over more of the TGT than the E5 experiment (Figures 6a and 6c). Finally, with $E_G = 1$, the G1 ice is everywhere stiffer (Figure 5e) and slower-flowing (Figures 6a and 6d) than E5. Our results suggest that accounting for the variation between extensional and simple shear stresses on the TGT is essential for the appropriate modification of ice stiffnesses.

On the slower-moving eastern portion of the ice shelf, all the flow relations overestimate the surface speeds and the magnitude of the overestimation increases with increasing overall enhancement, with the G1 simulated velocities best matching the observed (Figure 6; Table 2). The most likely cause of this overestimation is the mechanical linkage enforced in the model across the zone between the eastern shelf and the much faster TGT.

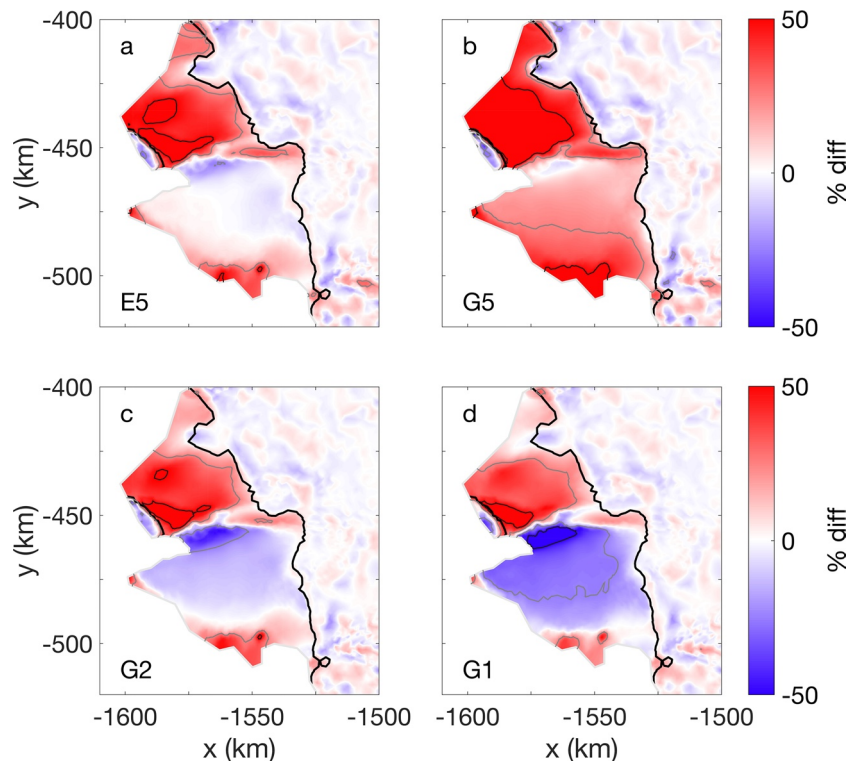


Figure 6. Percentage difference (modeled-observed) surface speeds for (a) E5; (b) G5; (c) G2; and (d) G1. The thick black line in each panel is the grounding line, and the thin black and gray lines are the $\pm 25\%$ and $\pm 50\%$ contours, respectively.

This linkage substantially increases the modeled eastern shelf speeds, in spite of the restraining effect of the pinning point at the ice-ocean front, and presumably also decreases the TGT speeds. That is, connection to the TGT drags the eastern shelf along, leading to overestimated speeds for each flow relation, and this overestimation on the eastern shelf occurs regardless of whether the speed of the faster moving TGT is close to observations (E5) or underestimated (G1).

5. Discussion

5.1. Modeled and Observed Deformation Regimes

To investigate the realism of the ESTAR and Glen deformation regimes over grounded ice, we consider the subglacial conditions of Thwaites—the topography, hydrology, thermal regime, and mechanics—which collectively provide insight on where sliding and deformational flow might occur.

In our diagnostic experiments over grounded ice, the flow relation determines the balance between basal sliding and deformation. Sliding naturally contributes less to overall flow as the enhancement of the deformational response to bed-parallel shear increases. This occurs for similar distributions of basal shear stresses between the flow relations, the magnitude of the basal shear stresses being determined predominantly by the common driving stress. The basal shear stress extrema also decrease with decreasing enhancement due to the relatively more important role of the membrane stresses in momentum balance as a result of stiffer ice. It follows that over grounded ice the largest differences in the relative contributions of deformational and sliding flow between the ESTAR and Glen flow relations arise where the basal shear stress magnitudes are larger and generally balance the local driving stresses (i.e., regions with “strong” beds; Joughin et al., 2009), which are mostly confined to the BDZ and DSZ.

Our models predict that the ice is frozen to the bed in most of the BDZ (Figure S4a and S4b in Supporting Information S1), except in localized zones of elevated geothermal heat flux (Figure S4c in Supporting Information S1; Schroeder, Blankenship, Young, & Quartini, 2014; Stål et al., 2021). Hence, flow is expected to be deformation-dominated in most of the BDZ, which is consistent with the E5 and G5 experiments, noting that the deformation speed fraction (Figure 3) naturally decreases with decreasing enhancement of simple shear. By contrast, G1 generally predicts widespread, unrealistic sliding-dominated flow in these regions.

For grounded ice we use inverse methods, matching observed and simulated surface speeds, to determine spatially-varying basal friction coefficients, and therefore the basal sliding velocities and balance between deformational and sliding flow. The friction coefficients we choose are non-unique (Text S2 in Supporting Information S1), although for each flow relation over the grounded ice sheet the modeled surface speeds are generally within 30 m yr^{-1} of the observations (except in the approach to the grounding line in the DSZ; Figure S2 in Supporting Information S1). Fine-tuning the cost function for the inversion scheme could marginally alter the details of the basal shear stress pattern. However, to produce deformation-dominated flow across the BDZ using the G1 flow relation, while still providing a satisfactory match to the observed surface velocities (via deformation), would require much larger basal shear stresses over broad areas. This is physically inconsistent with solution of the momentum balance equations forced by the observed driving stresses. Hence, our results in the BDZ demonstrate the inability of the G1 experiment to generate realistic and sufficient bed-parallel shear in regions where deformational flow should be significant or even dominant. While there are uncertainties in the simulated englacial temperature distribution, geothermal heat flux field, ice surface temperature, and temperature-dependent flow rate parameterization for $A(T)$ (see Text S3 in Supporting Information S1), this does constitute a major limitation for the standard Glen flow relation.

Elsewhere in the catchment, radar evidence supports the presence of subglacial melt water (Schroeder et al., 2013). In the DSZ, this subglacial hydrology is suggested to be in the form of a network of concentrated subglacial meltwater channels. Theory predicts that such channelized hydrological systems decrease basal lubrication compared with a distributed system, and can be present in areas with significant basal shear stresses (Creys & Schoof, 2009; Walder & Fowler, 1994). (Schroeder, Blankenship, Young, Witus, & Anderson, 2014) used airborne radar sounding to show that this region is characterized by a strong, rough bed consistent with outcropping bedrock. This suggests the existence of large basal shear stresses here, which is consistent with our findings for each of the flow relations.

In the fastest-flowing regions of the DSZ, the E5 and G5 experiments show localized high basal shear stresses and corresponding high rates of bed-parallel shear deformation. This result may have implications for local bed controls on patterns and rates of grounding line retreat, and is potentially relevant for other glaciers that are undergoing retreat, for example, in the Amundsen Sea sector (Joughin et al., 2014, 2019; Scheuchl et al., 2016; Seroussi et al., 2017). This finding warrants further attention, including into the coupled feedbacks between the thermo-mechanics of the ice sheet and subglacial hydrological network, and the implications of these feedbacks on thermal instabilities (see e.g., Mantelli et al., 2019; Mantelli & Schoof, 2019), using ice flow relations that account for tertiary creep.

In the SLZ, radar evidence indicates a widespread distributed subglacial hydrological system (Schroeder et al., 2013) as well as flow-aligned corrugated bedforms consistent with deformable sediments (Schroeder, Blankenship, Young, Witus, & Anderson, 2014). Consistent with theory (Creys & Schoof, 2009; Walder & Fowler, 1994), each of our flow relations predicts essentially plug flow across the SLZ. Schroeder et al. (2013) further delineated zones of depressed bed topography and substantial meltwater ponding (e.g., directly upstream of a topographic ridge transverse to flow south of the 76°S parallel), with corresponding low basal normal effective stress and basal friction expected. These zones directly correspond with the isolated pockets of almost vanishing basal shear stresses in our models, where momentum balance cannot be achieved by local processes alone, but requires higher magnitude and longer-range membrane stresses. The location of the transition from the distributed to the channelized subglacial hydrology network in Schroeder et al. (2013) also aligns very well with the transition from the SLZ to the DSZ in our E5 and G5 experiments.

For the floating ice shelf there is no basal friction and we also do not use an inversion approach to adjust the flow rate parameter A (T'), which would mask the impact of the different enhancement factors on modeled flow (Text S3 in Supporting Information S1). Hence, the ice shelf results for the different flow relations can be directly compared with observations. Here, the E5 experiment provides a better match to observations of the TGT than the enhanced or standard Glen flow relations. This is due to the ESTAR flow relation accounting for tertiary creep rates and particularly for the spatial differences in enhanced deformation inherent to ice anisotropy, parameterized through connection with the regional stress configuration. We note that other effects not included in the ESTAR flow relation, such as rifting or damage in a high shear stress environment, may also influence the flow regime of the TGT; in such scenarios it is possible that ESTAR predicts softening partly for the wrong reason.

By contrast with the TGT, all of the flow relations overestimate surface speeds on the eastern portion of the ice shelf. This might be because the model enforces a mechanical linkage between the TGT and the eastern portion of the ice shelf. In reality, the zone between the eastern and western portions of the ice shelf is extensively crevassed (Krabill, 2014; Lhermitte et al., 2020; Yu et al., 2017), and the strength of the mechanical linkages between the two portions of the ice shelf shows considerable variations over the period 2000 to 2018 (Miles et al., 2020). It is possible that for the time period represented in the surface velocity observations used here, there was a weaker transmission of stresses between the TGT and the eastern shelf than captured by our models. The assumption of visco-plastic deformation in this zone, as described by the flow relations used here, is also likely inapplicable, especially since non-rheological effects that influence flow, such as damage (Borstad et al., 2013), are not incorporated. Hence, it might be worthwhile to explore introducing a local “damage” factor (Borstad et al., 2013; C. Borstad et al., 2016) along the large velocity gradient between the eastern and western portions of the shelf in combination with the ESTAR flow relation.

5.2. Limitations Regarding Compatible Anisotropy

Graham et al. (2018) discussed the domain of applicability of the ESTAR flow relation, highlighting situations where the assumptions of tertiary creep and the establishment of compatible anisotropy might not apply. In the Thwaites catchment, we find localized regions where rapid and marked changes in dynamic conditions lead to similarly abrupt changes in applied stresses, which may result in the ice microstructure being locally incompatible with the stress configuration. Such situations include: (a) The grounding zone; (b) regions of variable basal shear stresses with abrupt transitions from shear stress-dominated to normal stress-dominated configurations; (c) regions where the membrane stresses vary, even where the basal stress configurations remain shear-dominated, and particularly where ice passes through the shear-dominated margins into areas of streaming flow. Since the enhancement factor E (λ_s) adjusts instantly to changes in the shear parameter, the predicted rheological properties may be inappropriate in each of these regions. Here, we address whether these local failures significantly

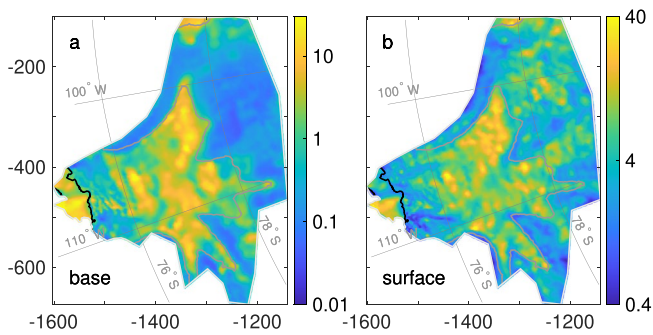


Figure 7. Distance (L ; km) to establish compatibility between stress configuration and ice crystal fabric for the ice (a) base and (b) surface. The black and gray lines in each panel are the same as in Figure 2. Note the different scales of the log color axes in each panel.

undermine the advantages that ESTAR has in capturing the dynamics elsewhere in the domain, and explore the regional extent of any incompatibility. Beyond this, there remains the open question of what rheological properties apply when an incompatible microstructure and stress configuration coexist, a consideration also absent in the Glen flow relation.

To assess the significance of regions of incompatibility, we estimate the distance L following an abrupt stress configuration change that is required to re-establish compatibility. As discussed in Graham et al. (2018), this is the distance ice travels while developing a compatible anisotropic crystal fabric under a presumed persistent flow regime. It depends on the time taken to produce total accumulated strain ϵ_D , given the magnitude of strain-rates represented by $\dot{\epsilon}_e$, and the ice velocity $|v|$. Hence,

$$L = |v|\epsilon_D/\dot{\epsilon}_e. \quad (7)$$

Laboratory experiments suggest that for initially isotropic ice, 10% strain is sufficient to establish tertiary flow and the compatible mechanical anisotropy (Budd & Jacka, 1989; Montagnat et al., 2009; Poirier, 1985; Schulson & Duval, 2009; Treverrow et al., 2012). However, in cases of smooth evolution of the shear parameter along flow, smaller deformations may achieve the new compatible state.

We assume $\epsilon_D = 10\%$, for a conservative estimate, and calculate L at the ice surface (L_s) and base (L_b). Across the grounded ice sheet, the compatibility lengths are generally much shorter in the basal layers (Figure 7a) than in the surface layers (Figure 7b), as expected, except in regions of plug flow where $L_s = L_b$. Both L_b and L_s are largest in the SLZ, explained by the increasing velocities and low effective strain rates here. Throughout most of the BDZ and DSZ, L_s is generally less than 10 km and L_b less than 1 km.

One clear class of abrupt transition in stress configuration captured by the basal λ_S^2 (Figure 2a) occurs at the grounding line, where it is predominantly isolated to the lower, warmer layers of the ice shelf. Here, we expect that compatibility is restored within approximately 10 km (Figure 7). In any case, the warmer, more deformable basal ice may not be important in controlling the momentum balance of the ice shelf, irrespective of the appropriateness of the abrupt change in basal enhancement produced in ESTAR at the grounding line.

A second class of abrupt transition occurs in the DSZ and SLZ where the basal shear stresses are variable, with transitions between shear and normal stress-dominated stress configurations. In particular, in zones of near-vanishing basal shear stresses where the basal shear parameter (Figure 2a) abruptly decreases, we observe that L_b correspondingly achieves local maxima. This scenario is potentially significant for incompatibility in the ESTAR assumptions, particularly given that there would not be significant fabric evolution across these highly localized regions. However, once again, the deformability of the basal ice here may be unimportant in the dynamics. The return to a shear-dominated basal stress configuration is typically associated with considerable shear stress and deformation, leading to basal compatibility distances that are often sub-kilometer (median $L_b = 692$ m in the DSZ). In the SLZ, the isolated regions of low basal shear parameter are more extensive than in the DSZ, although the patterns in dynamics in these zones are consistent. While local maxima in L are largest in the SLZ, it is important to remember that long compatibility scales are significant only where the shear fraction varies along the flow.

The third class of potential incompatibility issues occurs where the basal stress configuration remains relatively constant, but variations in λ_S (Figure 2b) may affect the membrane stresses. Such a scenario arises in the western shear margin of the DSZ, where horizontal simple shear becomes dominant. Here, the surface effective strain rates are large and the L_s and L_b values small, indicating that compatibility would be re-established relatively quickly. A similar pattern is evident in the slower-moving eastern region of the DSZ.

A special case of this third class concerns the shear-dominated margins, where ice enters regions of streaming flow. In these situations, the basal λ_S^2 values remain constant, but the surface λ_S^2 values increase on entering the shear margin and then decrease on leaving it (Figure 2a and 2b). While compatibility scales associated with entering the shear margin are low due to the high effective strain-rates in the membrane stresses, this is not the case for the exit into the streaming flow. For example, this occurs in the transition from the shear margin in the BDZ to the SLZ at approximately 107° W where the basal shear stresses are greater than 40 kPa in the SLZ. The low

surface strain rates in these regions of the SLZ lead to longer compatibility scales (Figure 7b). However, these low strain rates might mean that the instant switching to a stiffer ice enhancement factor (closer to E_C than E_S) may be relatively unimportant for the upper layers of the ice sheet compared to the higher viscosity (Figure 4c) associated with those low strain rates.

5.3. Other Limitations of ESTAR

Beyond the matter of compatible anisotropy, the ESTAR flow relation has other potential limitations in this application to the Thwaites Glacier catchment. Englacial temperatures in our model domain are not extreme by Antarctic standards, but do reach $\sim -30^\circ\text{C}$ in the interior of the catchment. From the conceptual overview in Section 2.1, there are two main aspects that deserve consideration.

First, as previously discussed, the deformability of colder ice under compression may be somewhat overestimated by our choice for E_C , due to the changing character of the compatible crystal orientation fabrics with decreasing temperature. It is difficult to assign a definitive temperature limit for ESTAR, since low temperature laboratory compression experiments only reach about 20% axial strain, so the conditions for a transition to a compatible fabric that might be stiff under compression (i.e., $E_C < 1$), that is, strong single maximum fabric, remain unknown. As discussed in Section 2.1, at low temperatures there may also be a long transient phase where the evolving crystal orientations are still relatively favorable for enhanced flow: a “quasi-compatibility.”

Temperatures throughout the Thwaites Ice Shelf are warmer than -14°C , while almost the entire DSZ is above -25°C , as is 95% of the lowest 30% of the SLZ. In the BDZ the stress regime is already strongly dominated by simple shear by mid-depth in the ice sheet so that, within the context of ESTAR, any overestimation of enhancement for compression in the colder upper layers may be of minor importance, considering the already high surface viscosities (Figures 4c, 4f, 4i and 4l).

Accordingly, we consider the parameterization taken for ESTAR, specifically the choice of $E_C > 1$, should be reasonable for most of the Thwaites domain. Furthermore, the greater enhancement of deformation under simple shear is a distinctive feature, and choosing a lower value for E_C would increase the contrast compared with our choice $E_C/E_S = 3/8$. The prospect that this contrast should be greater at the lowest temperatures is no reason to prefer the Glen relation.

There is a second limitation, which ESTAR shares with the Glen flow relation and the CAFFE model. As discussed in Section 2.1, at lower temperatures the assumption of a scalar flow relation will eventually fail, given the apparent trend in compatible fabrics toward a single maximum fabric compatible with both simple shear and compression on the shear plane. Transient experiments show that concentrated single maximum fabrics are soft under simple shear but stiff under compression, unlike the situation observed by Budd et al. (2013) that motivated ESTAR from their specific experimental geometry. At best, near the two extremes of simple shear or compression dominance, $E(\lambda_s)$ (Equation 3) assigns all components the enhancement factor for the predominant stress by interpolating between assigned values for E_C and E_S . The CAFFE model shares this limitation, with its deformability parameter (which links the stress tensor to the anisotropy) controlling its common enhancement factor. Both options appear more realistic than the Glen flow relation. Even with the limitations of a scalar flow relation we regard this as a step toward greater realism, as evidenced by our results comparing ESTAR and the unenhanced Glen flow relation in the BDZ and for the Thwaites Glacier Tongue, where ESTAR demonstrates a more realistic representation of the observed velocities, without any tuning of rate factors.

6. Conclusions

This study investigated the influence of ice flow relations on the modeled flow regime of Thwaites Glacier, comparing the ESTAR flow relation with the Glen flow relation. The ESTAR and Glen flow relations show significant differences in the contribution to ice motion from modeled bed-parallel shear deformations over the grounded Thwaites catchment. Quantitatively, we find: Median 57.6% more deformational contribution to surface velocity in E5 than G1; 38.2% more from deformation in E5 than G2; 8.7% less from deformation in E5 than G5. These differences are a consequence of the different enhancement factors and also (to a lesser extent) differing bed-parallel vertical shear stresses. The latter are reflected in the differing apportioning of the resistive forces (basal shear stresses and membrane stresses) that oppose gravitational driving in ice sheet dynamics. These

findings may be of particular importance—both at Thwaites Glacier and ice sheets and shelves everywhere—in understanding and predicting several aspects of the dynamics: The balance between sliding and deformational flow; how stresses are distributed; and how the ice geometry evolves in response to details at the bed, for example, near grounding lines and at the onset of sliding. ESTAR also captures better the patterns in surface speed over Thwaites Glacier Tongue. The ESTAR flow relation shows promise of more realistic simulations than the Glen flow relation because it captures the effects arising from accounting for tertiary creep rates and the spatially varying influence of flow-induced, compatible anisotropy on the modeled deformability of ice.

The study highlights a number of avenues for future exploration, including for ice shelves, where there is no complication from basal drag. The question of ice deformation in scenarios that do not meet the conditions of compatible anisotropy also requires further attention. This includes exploring the prevalence of such occurrences in ice sheets, the flow relations that might be applicable, and whether these situations represent significant localized controls on dynamics. Our results motivate the use of more complex flow relations such as the ESTAR flow relation that offer a more physically relevant treatment of deformation than the Glen flow relation at little additional computational cost, and further investigation of the consequences of using such relations in transient experiments of ice sheet dynamics.

Conflict of Interest

The authors declare no conflicts of interest relevant to this study.

Data Availability Statement

All of the data sets and source code used in this study are publicly available. We use version 4.19 of the open source ISSM software, which is freely available for download from <https://issm.jpl.nasa.gov/>. All the model initialization datasets used in this study are already available and are cited in this paper and its supporting information file.

References

- Aschwanden, A., Aoualgeirsdóttir, G., & Khroulev, C. (2013). Hindcasting to measure ice sheet model sensitivity to initial states. *The Cryosphere*, 7, 1083–1093. <https://doi.org/10.5194/tc-7-1083-2013>
- Aschwanden, A., Bueller, E., Khroulev, C., & Blatter, H. (2012). An enthalpy formulation for glaciers and ice sheets. *Journal of Glaciology*, 58(209), 441–457. <https://doi.org/10.3189/2012JG11J088>
- Azuma, N., & Goto-Azuma, K. (1996). An anisotropic flow law for ice sheet ice and its implications. *Annals of Glaciology*, 23, 202–208. <https://doi.org/10.3189/s0260305500013458>
- Bindschadler, R. A., Nowicki, S., Abe-Ouchi, A., Aschwanden, A., Choi, H., Fastook, J., et al. (2013). Ice-sheet model sensitivities to environmental forcing and their use in projecting future sea-level (the SeaRISE project). *Journal of Glaciology*, 59(214), 195–224. <https://doi.org/10.3189/2013JG12J125>
- Blatter, H. (1995). Velocity and stress-fields in grounded glaciers: A simple algorithm for including deviatoric stress gradients. *Journal of Glaciology*, 41(138), 333–344. <https://doi.org/10.3189/S002214300001621X>
- Bons, P. D., Jansen, D., Mundel, F., Bauer, C. C., Binder, T., Eisen, O., et al. (2016). Converging flow and anisotropy cause large-scale folding in Greenland's ice sheet. *Nature Communications*, 7(11427). <https://doi.org/10.1038/ncomms11427>
- Borstad, C., Khazendar, A., Scheuchl, B., Morlighem, M., Larour, E., & Rignot, E. (2016). A constitutive framework for predicting weakening and reduced buttressing of ice shelves based on observations of the progressive deterioration of the remnant Larsen B ice shelf. *Geophysical Research Letters*, 43(5), 2027–2035. <https://doi.org/10.1002/2015GL067365>
- Borstad, C. P., Rignot, E., Mouginot, J., & Schodlok, M. P. (2013). Creep deformation and buttressing capacity of damaged ice shelves: Theory and application to Larsen C ice shelf. *The Cryosphere*, 7(6), 1931–1947. <https://doi.org/10.5194/tc-7-1931-2013>
- Budd, W. F., & Jacka, T. H. (1989). A review of ice rheology for ice sheet modelling. *Cold Regions Science and Technology*, 16(2), 107–144. [https://doi.org/10.1016/0165-232X\(89\)90014-1](https://doi.org/10.1016/0165-232X(89)90014-1)
- Budd, W. F., Keage, P. L., & Blundy, N. A. (1979). Empirical studies of ice sliding. *Journal of Glaciology*, 23(89), 157–170. <https://doi.org/10.3189/S0022143000029804>
- Budd, W. F., Warner, R. C., Jacka, T. H., Li, J., & Treverrow, A. (2013). Ice flow relations for stress and strain-rate components from combined shear and compression laboratory experiments. *Journal of Glaciology*, 59(214), 374–392. <https://doi.org/10.3189/2013JG12J106>
- Craw, L., Qi, C., Prior, D. J., Goldsby, D. L., & Kim, D. (2018). Mechanics and microstructure of deformed natural anisotropic ice. *Journal of Structural Geology*, 115, 152–166. <https://doi.org/10.1016/j.jsg.2018.07.014>
- Creys, T. T., & Schoof, C. G. (2009). Drainage through subglacial water sheets. *Journal of Geophysical Research*, 114, 1–18. <https://doi.org/10.1029/2008JF001215>
- Cuffey, K., & Paterson, W. S. B. (2010). In Butterworth-Heinemann (Ed.), *The physics of glaciers* (4th ed.). Elsevier.
- Dahl-Jensen, D., Thorsteinsson, T., Alley, R., & Shoji, H. (1997). Flow properties of the ice from the Greenland ice core project ice core: The reason for folds? *Journal of Geophysical Research*, 102(C12), 26831–26840. <https://doi.org/10.1029/97JC01266>
- Duval, P. (1981). Creep and fabrics of polycrystalline ice under shear and compression. *Journal of Glaciology*, 27(95), 129–140. <https://doi.org/10.3189/S002214300001128X>

Acknowledgments

The authors thank four reviewers whose comments and suggestions led to a much improved manuscript. The research was supported under the Australian Research Council's Special Research Initiative for Antarctic Gateway Partnership (Project ID SR140300001), and the Australian Government's Cooperative Research Centers Programme through the Antarctic Climate & Ecosystems Cooperative Research Center (ACE CRC). F. McCormack was supported by an Australian Research Council Discovery Early Career Award (DE210101433). This research was undertaken with the assistance of resources from the National Computational Infrastructure, which is supported by the Australian Government and the Tasmanian Partnership for Advanced Computing. H. Seroussi was funded by grants from NASA Cryospheric Science and Modeling, Analysis, Prediction Programs. C. Dow was supported by the Canada Research Chairs Program (950-231237). This project received grant funding from the Australian Government as part of the Antarctic Science Collaboration Initiative program. Lastly, the authors acknowledge the influence of the late William (Bill) Francis Budd (1938–2022): from discussions and advice about the present work, to his long-term contributions to the studies of ice deformation, including the program of work that led to the ESTAR flow relation. RW and AT particularly want to thank Bill for many years of friendly and inspirational collaboration. Open access publishing facilitated by Monash University, as part of the Wiley - Monash University agreement via the Council of Australian University Librarians.

- Fan, S., Hager, T. F., Prior, D. J., Cross, A. J., Goldsby, D. L., Qi, C., et al. (2020). Temperature and strain controls on ice deformation mechanisms: Insights from the microstructures of samples deformed to progressively higher strains at -10 , -20 and -30°C . *The Cryosphere*, *14*, 3875–3905. <https://doi.org/10.5194/tc-14-3875-2020>
- Faria, S. H., Weikusat, L., & Azuma, N. (2014a). The microstructure of polar ice. Part I: Highlights from ice core research. *Journal of Structural Geology*, *61*, 2–20. <https://doi.org/10.1016/j.jsg.2013.09.010>
- Faria, S. H., Weikusat, L., & Azuma, N. (2014b). The microstructure of polar ice. Part II: Start of the art. *Journal of Structural Geology*, *61*, 21–49. <https://doi.org/10.1016/j.jsg.2013.11.003>
- Gardner, A. S., Moholdt, G., Scambos, T., Fahnestock, M., Ligtenberg, S., van den Broeke, M., & Nilsson, J. (2018). Increased West Antarctic and unchanged East Antarctic ice discharge over the last 7 years. *The Cryosphere*, *12*(2), 521–547. <https://doi.org/10.5194/tc-12-521-2018>
- Gillet-Chaulet, F., Gagliardini, O., Meyssonier, J., Montagnat, M., & Castelnau, O. (2005). A user-friendly anisotropic flow law for ice-sheet modelling (Article). *Journal of Glaciology*, *51*(172), 3–14. <https://doi.org/10.3189/172756505781829584>
- Gillet-Chaulet, F., Gagliardini, O., Meyssonier, J., Zwinger, T., & Ruokolainen, J. (2006). Flow-induced anisotropy in polar ice and related ice-sheet flow modelling. *Journal of Non-Newtonian Fluid Mechanics*, *134*, 33–43. <https://doi.org/10.1016/j.jnnfm.2005.11.005>
- Glen, J. W. (1952). Experiments on the deformation of ice. *Journal of Glaciology*, *2*(12), 111–114. <https://doi.org/10.3189/S0022143000034067>
- Glen, J. W. (1953). Rate of flow of polycrystalline ice. *Nature*, *172*(4381), 721–722. <https://doi.org/10.1038/172721a0>
- Glen, J. W. (1955). The creep of polycrystalline ice. *Proceedings of the Royal Society A*, *228*(1175), 519–538. <https://doi.org/10.1098/rspa.1955.0066>
- Glen, J. W. (1958). *The flow law of ice: A discussion of the assumptions made in glacier theory, their experimental foundations and consequences* (Vol. 47, pp. 171–183). International Association of Hydrological Sciences Publication.
- Graham, F., Morlighem, M., Warner, R., & Treverrow, A. (2018). Implementing an empirical scalar constitutive relation for ice with flow-induced polycrystalline anisotropy in large-scale ice sheet models. *The Cryosphere*, *12*, 1047–1067. <https://doi.org/10.5194/tc-12-1047-2018>
- Greve, R., & Blatter, H. (2009). *Dynamics of ice sheets and glaciers*. Springer-Verlag.
- Greve, R., & Hutter, K. (1995). Polythermal three-dimensional modelling of the Greenland ice sheet with varied geothermal heat flux. *Annals of Glaciology*, *21*, 8–12. <https://doi.org/10.3189/S0260305500015524>
- Greve, R., Zwinger, T., & Gong, Y. (2014). On the pressure dependence of the rate factor in Glen's flow law. *Journal of Glaciology*, *60*(220), 397–399. <https://doi.org/10.3189/2014JoG14J019>
- Hansen, P. C. (2000). The L-curve and its use in the numerical treatment of inverse problems. In P. Johnston (Ed.), *Computational inverse problems in electrocardiology. Advances in computational bioengineering* (pp. 119–142). WIT Press.
- Hindmarsh, R. C. A. (2006). The role of membrane-like stresses in determining the stability and sensitivity of the Antarctic ice sheets: Back pressure and grounding line motion. *Philosophical Transactions of the Royal Society of London—A*, *364*(1844), 1733–1767. <https://doi.org/10.1098/rsta.2006.1797>
- Huybrechts, P., & Oerlemans, J. (1988). Evolution of the East Antarctic ice sheet: A numerical study of thermo-mechanical response patterns with changing climate. *Annals of Glaciology*, *11*, 52–59. <https://doi.org/10.3189/S0260305500006327>
- Jacka, T. H., & Jun, L. (2000). Flow rates and crystal orientation fabrics in compression of polycrystalline ice at low temperatures and stresses. In T. Hondoh (Ed.), *Physics of ice core records* (pp. 83–102). Hokkaido University Press.
- Jezek, K., & Team, R. P. (2002). RAMP AMM-1 SAR image mosaic of Antarctica version 2. Fairbanks, AK: Alaska satellite facility. Center in association with the national snow and ice data.
- Jordan, T. M., Schroeder, D. M., Castelletti, D., Li, J., & Dall, J. (2019). A polarimetric coherence method to determine ice crystal orientation fabric from radar sounding: Application to the NEEM ice core region. *IEEE Transactions on Geoscience and Remote Sensing*, *57*(11), 8641–8657. <https://doi.org/10.1109/TGRS.2019.2921980>
- Joughin, I., Smith, B. E., & Medley, B. (2014). Marine ice sheet collapse potentially underway for the Thwaites Glacier Basin, West Antarctica. *Science*, *344*(6185), 735–738. <https://doi.org/10.1126/science.1249055>
- Joughin, I., Smith, B. E., & Schoof, C. G. (2019). Regularized Coulomb friction laws for ice sheet sliding: Application to Pine Island glacier, Antarctica. *Geophysical Research Letters*, *46*(9), 4764–4771. <https://doi.org/10.1029/2019GL082526>
- Joughin, I., Tulaczyk, S., Bamber, J., Blankenship, D., Holt, J., Scambos, T., & Vaughan, D. (2009). Basal conditions for Pine Island and Thwaites glaciers, West Antarctica, determined using satellite and airborne data. *Journal of Glaciology*, *55*(190), 245–257. <https://doi.org/10.3189/002214309788608705>
- Kamb, B. (1972). Experimental recrystallization of ice under stress. In *Flow and fracture of rocks* (pp. 211–241). American Geophysical Union (AGU). <https://doi.org/10.1029/GM016p0211>
- Krabill, W. B. (2014). *IceBridge ATM L2 ICESat elevation, slope, and roughness, version 2*. NASA Distrib. Active Archive Center, Nat. Snow Ice Data Center.
- Larour, E., Seroussi, H., Morlighem, M., & Rignot, E. (2012). Continental scale, high order, high spatial resolution, ice sheet modeling using the Ice sheet system model (ISSM). *Journal of Geophysical Research*, *117*(F01022). <https://doi.org/10.1029/2011JF002140>
- Lenaerts, J. T. M., van den Broeke, M. R., van Angelen, J. H., van Meijgaard, E., & Dery, S. J. (2012). Drifting snow climate of the Greenland ice sheet: A study with a regional climate model. *The Cryosphere*, *6*(4), 891–899. <https://doi.org/10.5194/tc-6-891-2012>
- Lhermitte, S., Sun, S., Shuman, C., Wouters, B., Pattyn, F., Wuite, J., et al. (2020). Damage accelerates ice shelf instability and mass loss in Amundsen Sea embayment. *Proceedings of the National Academy of Sciences*, *117*(40), 24735–24741. <https://doi.org/10.1073/pnas.1912890117>
- Li, J., Jacka, J., & Budd, W. F. (1996). Deformation rates in combined compression and shear for ice which is initially isotropic and after the development of strong anisotropy. *Annals of Glaciology*, *23*, 247–252. <https://doi.org/10.3189/S0260305500013501>
- Lipenkov, V. Y., Barkov, N. I., Duval, P., & Pimienta, P. (1989). Crystalline texture of the 2083 m ice core at Vostok Station, Antarctica. *Journal of Glaciology*, *35*, 392–398. <https://doi.org/10.3189/S0022143000009321>
- Maijer, N., Humphrey, N., Harper, J., & Meierbachtol, T. (2019). Sliding dominates slow-flowing margin regions, Greenland Ice Sheet. *Science Advances*, *5*(eaaw5406). <https://doi.org/10.1126/sciadv.aaw5406>
- Mantelli, E., Haseloff, M., & Schoof, C. (2019). Ice sheet flow with thermally activated sliding. Part 1: The role of advection. *Proceedings of the Royal Society A*, *475*(2230). <https://doi.org/10.1098/rspa.2019.0410>
- Mantelli, E., & Schoof, C. (2019). Ice sheet flow with thermally activated sliding. Part 2: The stability of subtemperate regions. *Proceedings of the Royal Society A*, *475*(2231). <https://doi.org/10.1098/rspa.2019.0411>
- Marshall, S. J. (2005). Recent advances in understanding ice sheet dynamics. *Earth and Planetary Science Letters*, *240*, 191–204. <https://doi.org/10.1016/j.epsl.2005.08.016>
- Martin, M. A., Winkelmann, R., Haseloff, M., Albrecht, T., Bueler, E., Khroulev, C., & Levermann, A. (2011). The Potsdam parallel ice sheet model (PISM-PIK)—Part 2: Dynamic equilibrium simulation of the Antarctic ice sheet. *The Cryosphere*, *5*(3), 727–740. <https://doi.org/10.5194/tc-5-727-2011>

- Miles, B. W. J., Stokes, C. R., Jenkins, A., Jordan, J. R., Jamieson, S. S. R., & Gudmundsson, G. H. (2020). Intermittent structural weakening and acceleration of the Thwaites Glacier tongue between 2000 and 2018. *Journal of Glaciology*, 66(257), 485–495. <https://doi.org/10.1017/jog.2020.20>
- Milillo, P., Rignot, E., Rizzoli, P., Scheuchl, B., Mouginot, J., Bueso-Bello, J., & Prats-Iraola, P. (2019). Heterogeneous retreat and ice melt of Thwaites Glacier, West Antarctica. *Science Advances*, 5(1). eaau3433. <https://doi.org/10.1126/sciadv.aau3433>
- Minchew, B. M., Meyer, C. R., Robel, A. A., Gudmundsson, G. H., & Simons, M. (2018). Processes controlling the downstream evolution of ice rheology in glacier shear margins: Case study on Rutford ice stream, West Antarctica. *Journal of Glaciology*, 64(246), 1–594. <https://doi.org/10.1017/jog.2018.47>
- Montagnat, M., Durand, G., & Duval, P. (2009). Recrystallization processes in granular ice. In T. Hondoh (Ed.), *Physics of ice core records II*. Hokkaido University Press. (Supplement Issue of Low Temperature Science 68).
- Morlighem, M., Rignot, E., Binder, T., Blankenship, D., Drews, R., Eagles, G., et al. (2020). Deep glacial troughs and stabilizing ridges unveiled beneath the margins of the Antarctic ice sheet. *Nature Geoscience*, 13, 132–137. <https://doi.org/10.1038/s41561-019-0510-8>
- Morlighem, M., Rignot, E., Seroussi, H., Larour, E., Ben Dhia, H., & Aubry, D. (2010). Spatial patterns of basal drag inferred using control methods from a full-Stokes and simpler models for Pine Island glacier, West Antarctica. *Geophysical Research Letters*, 37(L14502). <https://doi.org/10.1029/2010GL043853>
- Mouginot, J., Rignot, E., & Scheuchl, B. (2014). Sustained increase in ice discharge from the Amundsen Sea embayment, West Antarctica, from 1973 to 2013. *Geophysical Research Letters*, 41, 1–1584. <https://doi.org/10.1002/2013GL059069>
- Nye, J. F. (1953). The flow law of ice from measurements in glacier tunnels, laboratory experiments and the Jungfraufirn borehole experiment. *Proceedings of the Royal Society A*, 219(1193), 477–489. <https://doi.org/10.1098/rspa.1953.0161>
- Paolo, F., Fricker, H., & Padman, L. (2015). Volume loss from Antarctic ice shelves is accelerating. *Science*, 348, 327–331. <https://doi.org/10.1126/science.aaa0940>
- Paterson, W. S. B. (1994). In B. Heinemann (Ed.), *The physics of glaciers* (3rd ed.). Pergamon Press.
- Pattyn, F. (2003). A new three-dimensional higher-order thermomechanical ice sheet model: Basic sensitivity, ice stream development, and ice flow across subglacial lakes. *Journal of Geophysical Research*, 108(B8), 1–15. <https://doi.org/10.1029/2002JB002329>
- Pimienta, P., Duval, P., & Lipenkov, V. Y. (1987). Mechanical behaviour of anisotropic polar ice. In E. D. Waddington, & J. S. Walder (Eds.), *The physical basis of ice sheet modelling* (pp. 57–66). IAHS Press.
- Placidi, L., Greve, R., Seddik, H., & Faria, S. H. (2010). Continuum-mechanical, Anisotropic Flow model for polar ice masses, based on an anisotropic flow enhancement factor. *Continuum Mechanics and Thermodynamics*, 22(3), 221–237. <https://doi.org/10.1007/s00161-009-0126-0>
- Placidi, L., & Hutter, K. (2006). An anisotropic flow law for incompressible polycrystalline materials. *Zeitschrift für Angewandte Mathematik und Physik*, 57(1), 160–181.
- Poirier, J.-P. (1985). *Creep of crystals: High-temperature deformation processes in metals, ceramics and minerals*. Cambridge University Press.
- Qi, C., Goldsby, D. L., & Prior, D. J. (2017). The down-stress transition from cluster to cone fabrics in experimentally deformed ice. *Earth and Planetary Science Letters*, 471, 136–147. <https://doi.org/10.1016/j.epsl.2017.05.008>
- Qi, C., Prior, D. J., Craw, L., Fan, S., Llorens, M.-G., Griera, A., et al. (2019). Crystallographic preferred orientations of ice deformed in direct-shear experiments at low temperatures. *Cryosphere*, 13, 351–371. <https://doi.org/10.5194/tc-13-351-2019>
- Raymond, C. F., Echelmeyer, K. A., Whillans, I. M., & Doake, C. S. M. (2001). Ice stream shear margins. In R. B. Alley, & R. A. Bindshadler (Eds.), *The West Antarctic ice sheet: Behavior and environment*. Antarctic research series (Vol. 77, pp. 137–155). American Geophysical Union.
- Richards, D. H. M., Pegler, S. S., Piazzolo, S., & Harlen, O. G. (2021). The evolution of ice fabrics: A continuum modelling approach validated against laboratory experiments. *Earth and Planetary Science Letters*, 556, 116718. <https://doi.org/10.1016/j.epsl.2020.116718>
- Rignot, E. (2001). Evidence for rapid retreat and mass loss of Thwaites Glacier, West Antarctica. *Journal of Glaciology*, 47(157), 213–222. <https://doi.org/10.3189/172756501781832340>
- Rignot, E. (2008). PALSAR studies of ice sheet motion in Antarctica. In *ALOS PI Symposium, November 3–7 2008*.
- Rignot, E., Mouginot, J., & Scheuchl, B. (2011). Ice flow of the Antarctic ice sheet. *Science*, 333(6048), 1427–1430. <https://doi.org/10.1126/science.1208336>
- Rignot, E., Mouginot, J., & Scheuchl, B. (2017). MEaSURES InSAR-based Antarctica ice velocity map 450 m Version 2.0. *NASA National Snow and Ice Data Center Distributed Active Archive Center*. <https://doi.org/10.5067/D7GK8F5J8M8R>
- Scambos, T. A., Bell, R. E., Alley, R. B., Anandakrishnan, S., Bromwich, D., Brunt, K., et al. (2017). How much, how fast? A science review and outlook for research on the instability of Antarctica's Thwaites Glacier in the 21st century. *Global and Planetary Change*, 153, 16–34. <https://doi.org/10.1016/j.gloplacha.2017.04.008>
- Scheuchl, B., Mouginot, J., Rignot, E., Morlighem, M., & Khazendar, A. (2016). Grounding line retreat of Pope, Smith, and Kohler glaciers, West Antarctica, measured with sentinel-1a radar interferometry data. *Geophysical Research Letters*, 43, 8572–8579. <https://doi.org/10.1002/2016GL069287>
- Schroeder, D. M., Blankenship, D. D., & Young, D. A. (2013). Evidence for a water system transition beneath Thwaites Glacier, West Antarctica. *Proceedings of the National Academy of Sciences*, 110(30), 12225–12228. <https://doi.org/10.1073/pnas.1302828110>
- Schroeder, D. M., Blankenship, D. D., Young, D. A., & Quartini, E. (2014). Evidence for elevated and spatially variable geothermal flux beneath the West Antarctic Ice Sheet. *Proceedings of the National Academy of Sciences*, 111(25), 9070–9072. <https://doi.org/10.1073/pnas.1405184111>
- Schroeder, D. M., Blankenship, D. D., Young, D. A., Witus, A. E., & Anderson, J. B. (2014). Airborne radar sounding evidence for deformable sediments and outcropping bedrock beneath Thwaites Glacier, West Antarctica. *Geophysical Research Letters*, 41, 7200–7208. <https://doi.org/10.1002/2014GL061645>
- Schulson, E., & Duval, P. (2009). *Creep and fracture of ice*. Cambridge University Press.
- Sergienko, O. V., Creyts, T. T., & Hindmarsh, R. C. A. (2014). Similarity of organized patterns in driving and basal stresses of Antarctic and Greenland ice sheets beneath extensive areas of basal sliding. *Geophysical Research Letters*, 41(11), 3925–3932. <https://doi.org/10.1002/2014gl059976>
- Sergienko, O. V., & Hindmarsh, R. C. A. (2013). Regular patterns in frictional resistance of ice-stream beds seen by surface data inversion. *Science*, 342(6162), 1086–1089. <https://doi.org/10.1126/science.1243903>
- Seroussi, H., Morlighem, M., Rignot, E., Khazendar, A., Larour, E., & Mouginot, J. (2013). Dependence of century-scale projections of the Greenland ice sheet on its thermal regime. *Journal of Glaciology*, 59(218), 1024–1034. <https://doi.org/10.3189/2013JoG13J054>
- Seroussi, H., Nakayama, Y., Larour, E., Menemenlis, D., Morlighem, M., Rignot, E., & Khazendar, A. (2017). Continued retreat of Thwaites Glacier, West Antarctica, controlled by bed topography and ocean circulation. *Geophysical Research Letters*, 44, 6191–6199. <https://doi.org/10.1002/2017GL072910>

- Smith, E. C., Baird, A. F., Kendall, J. M., Martín, C., White, R. S., Brisbourne, A. M., & Smith, A. M. (2017). Ice fabric in an Antarctic ice stream interpreted from seismic anisotropy. *Geophysical Research Letters*, *44*(8), 3710–3718. <https://doi.org/10.1002/2016gl072093>
- Stål, T., Reading, A. M., Halpin, J. A., & Whittaker, J. M. (2021). Antarctic geothermal heat flow model: Aq1. *Geochemistry, Geophysics, Geosystems*, *22*, e2020GC009428. <https://doi.org/10.1029/2020GC009428>
- Treverrow, A., Budd, W. F., Jacka, T. H., & Warner, R. C. (2012). The tertiary creep of polycrystalline ice: Experimental evidence for stress-dependent levels of strain-rate enhancement. *Journal of Glaciology*, *58*(208), 301–314. <https://doi.org/10.3189/2012JG11J149>
- Treverrow, A., Jun, L., & Jacka, T. H. (2016). Ice crystal c-axis orientation and mean grain size measurements from the Dome Summit South ice core, Law Dome, East Antarctica. *Earth System Science Data*, *8*(1), 253–263. <https://doi.org/10.5194/essd-8-253-2016>
- Treverrow, A., Warner, R. C., Budd, W. F., Jacka, T. H., & Roberts, J. L. (2015). Modelled stress distributions at the Dome Summit south borehole, Law Dome, East Antarctica: A comparison of anisotropic ice flow relations. *Journal of Glaciology*, *61*(229), 987–1004. <https://doi.org/10.3189/2015jog14j198>
- Walder, J. S., & Fowler, A. (1994). Channelized subglacial drainage over a deformable bed. *Journal of Glaciology*, *40*(134), 3–15. <https://doi.org/10.3189/S0022143000003750>
- Warner, R. C., Jacka, T. H., Li, J., & Budd, W. F. (1999). Tertiary flow relations for compression and shear components in combined stress tests on ice. In K. Hutter, Y. Wang, & H. Beer (Eds.), *Advances in cold-region thermal engineering and sciences: Technological, environmental, and climatological impact* (pp. 259–270). Springer-Verlag.
- Weertman, J. (1974). Stability of the junction of an ice sheet and an ice shelf. *Journal of Glaciology*, *13*(67), 3–11. <https://doi.org/10.3189/S0022143000023327>
- Weikusat, I., Jansen, D., Binder, T., Eichler, J., Faria, S. H., Wilhelms, F., et al. (2017). Physical analysis of an Antarctic ice core—towards an integration of micro- and macrodynamics of polar ice. *Philosophical Transactions of the Royal Society A*, *375*. <https://doi.org/10.1098/rsta.2015.0347>
- Yu, H., Rignot, E., Morlighem, M., & Seroussi, H. (2017). Iceberg calving of Thwaites Glacier, West Antarctica: Full-stokes modeling combined with linear elastic fracture mechanics. *The Cryosphere*, *11*(3), 1283–1296. <https://doi.org/10.5194/tc-11-1283-2017>
- Zeit, M., Levermann, A., & Winkelmann, R. (2020). Sensitivity of ice loss to uncertainty in flow law parameters in an idealized one-dimensional geometry. *Cryosphere*, *14*, 3537–3550. <https://doi.org/10.5194/tc-14-3537-2020>

References From the Supporting Information

- Morlighem, M., Seroussi, H., Larour, E., & Rignot, E. (2013). Inversion of basal friction in Antarctica using exact and incomplete adjoints of a higher-order model. *Journal of Geophysical Research*, *118*(3), 1746–1753. <https://doi.org/10.1002/jgrf.20125>
- Zhao, C., Gladstone, R. M., Warner, R. C., King, M. A., Zwinger, T., & Morlighem, M. (2018a). Basal friction of Fleming Glacier, Antarctica-Part 1: Sensitivity of inversion to temperature and bedrock uncertainty. *Cryosphere*, *12*, 2637–2652.
- Zhao, C., Gladstone, R. M., Warner, R. C., King, M. A., Zwinger, T., & Morlighem, M. (2018b). Basal friction of Fleming glacier, Antarctica-Part 2: Evolution from 2008 to 2015. *The Cryosphere*, *12*, 2653–2666. <https://doi.org/10.5194/tc-12-2653-2018>